nature physics

Article

https://doi.org/10.1038/s41567-023-02327-6

Ferroelectric and spontaneous quantum Hall states in intrinsic rhombohedral trilayer graphene

Received: 21 February 2023

Accepted: 8 November 2023

Published online: 16 January 2024

Check for updates

Felix Winterer [1], Fabian R. Geisenhof [1], Noelia Fernandez [1,2], Anna M. Seiler [1,2], Fan Zhang [3] ✉ & R. Thomas Weitz [1,2] ✉

Non-trivial interacting phases can emerge in elementary materials. As a prime example, continuing advances in device quality have facilitated the observation of a variety of spontaneously ordered quantum states in bilayer graphene. Its natural extension, rhombohedral trilayer graphene—in which the layers are stacked in an ABC fashion—is predicted to host stronger electron–electron interactions than bilayer graphene because of its flatter low-energy bands and larger winding number. Theoretically, five spontaneous quantum Hall phases have been proposed to be candidate electronic ground states. Here we observe evidence for four of the five competing ordered states in interaction-maximized, dual-gated, rhombohedral trilayer graphene. In particular, at small magnetic fields, two states with Chern numbers 3 and 6 can be stabilized at elevated and low perpendicular electric fields, respectively, and both exhibit clear magnetic hysteresis. We also show that the quantum Hall ferromagnets of the zero-energy Landau levels are ferroelectrics with spontaneous layer polarizations even at zero electric field, as evidenced by electric hysteresis.

The competition between kinetic and exchange energies in conjunction with the band topology determines the ground state properties of an interacting system. Recently, experiments featuring Chern insulator ground states in moiré superlattices without the requirement of applying any external magnetic field or magnetic dopant[1–5] have gained notable interest. In fact, two such quantum anomalous Hall (QAH) phases were predicted to be competing ground states of the naturally occurring rhombohedral graphene systems such as AB bilayer[6,7] and ABC trilayer[6,8]. Although consistent signatures have already been identified in a recent experimental examination of suspended AB bilayer graphene (BLG)[9], in principle, the susceptibility towards spontaneously gapped phases in ABC trilayer graphene (r-TLG) should be still stronger[8,10]. This is evident by comparing the experimental conditions to observe the unexpectedly discovered Stoner magnetism and unusual superconductivity in lightly hole-doped BLG[8,10–14] and r-TLG[15,16].

In rhombohedral multilayer graphene, quasiparticles can be described by a two-component pseudospinor associated with the two low-energy sublattice sites located respectively on the two outermost layers[6,8,17–19], leading to an effective two-touching-band Hamiltonian $H = \frac{(\upsilon_F p)^N}{\gamma_1^{N-1}}\left[\cos(N\phi)\,\sigma_x + \sin(N\phi)\,\sigma_y\right]$. (The trigonal warping effect can be appropriately ignored for this work; see also Supplementary Section 1.) Here, N is the number of layers, υ_F is the Fermi velocity in graphene, γ_1 is the nearest-neighbour interlayer hopping energy, p is the momentum with $\phi = \tan^{-1}\xi p_y/p_x$, $\xi = \pm 1$ labels the K and K′ valleys, and σ are the Pauli matrices acting on the layer pseudospin. A quasiparticle acquires a Berry phase of $\xi N\pi$ when encircling the band touching point at K or K′. The band touching nature and Berry phase quantization is protected by the sublattice or chiral symmetry and by the inversion and time-reversal symmetries[8]. Thus, a perpendicular electric field[18,19] or electron–electron interactions[6,8,19] can explicitly or

[1]Physics of Nanosystems, Department of Physics, Ludwig-Maximilians-Universität München, Munich, Germany. [2]1st Institute of Physics, Faculty of Physics, University of Göttingen, Göttingen, Germany. [3]Department of Physics, University of Texas at Dallas, Richardson, TX, USA. ✉e-mail: Zhang@utdallas.edu; thomas.weitz@uni-goettingen.de

https://doi.org/10.1038/s41567-023-02327-6

a

	K↑	K↓	K′↑	K′↓	Layer polarization	Total orbital magnetization	Charge Hall conductivity
QVH	T	T	T	T	Full	No	0
QAH	T	T	B	B	No	Yes	$6\,e^2\,h^{-1}$
LAF	T	B	T	B	No	No	0
QSH	T	B	B	T	No	No	0
ALL	T	T	T	B	Partial	Yes	$3\,e^2\,h^{-1}$

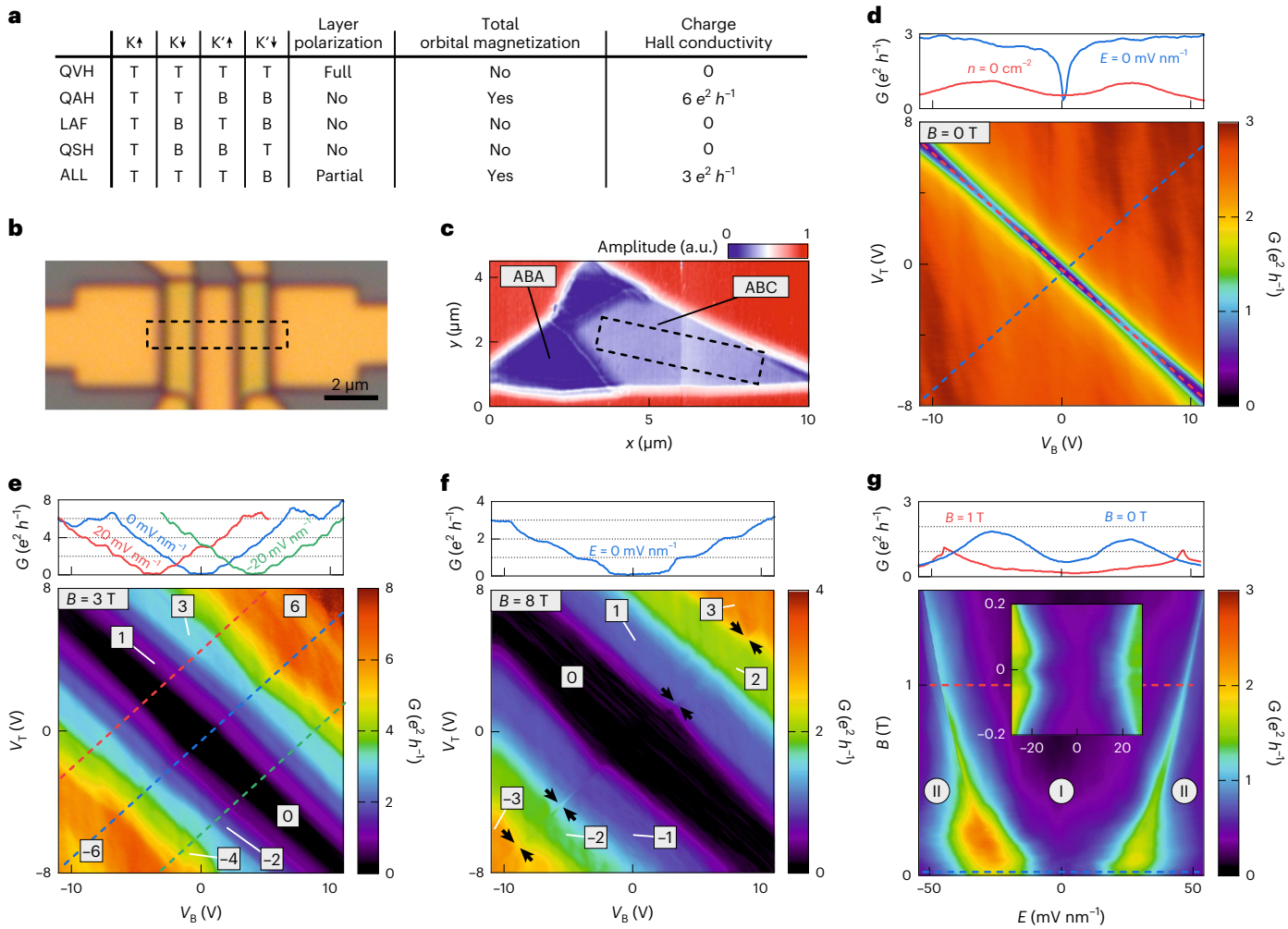

Fig. 1 | Microscopy and transport measurements. a, Overview of the five predicted spontaneous quantum Hall states in r-TLG with their corresponding layer polarizations (T for top and B for bottom), total orbital magnetizations and charge Hall conductivities. **b**,**c**, Optical microscopy image (**b**) of a suspended dual-gated r-TLG sample (black dotted box) together with the corresponding scattering scanning near-field optical microscopy image (**c**). The amplitude in **c** is given in arbitrary units (a.u.) and the vertical discontinuity in the ABC region is a measurement artefact. **d**–**f**, Differential conductance map as a function of top and bottom gate voltages at $B = 0$ T (**d**), $B = 3$ T (**e**) and $B = 8$ T (**f**). Landau-level filling factors are indicated by numerals. Line cuts (dotted lines in the contour plots) at constant charge carrier density n or electric field E are shown in the top panels. The dotted line at vanishing electric field is omitted in **f** for better visibility of the discontinuities in the conductance (marked by black arrows). **g**, Differential conductance map as a function of E and B at charge neutrality. Line cuts at constant B are shown in the top panel. The inset shows an enlarged image close to vanishing fields. The low conductance regions can be identified as the LAF/CAF (I) and QVH (II) phases.

spontaneously break the symmetry and open an energy gap. Moreover, rhombohedral multilayer graphene has a power-law dispersion $E \propto p^N$ that flattens with increasing N. This is reflected by the density of states (DOS) near charge neutrality that is proportional to $E^{(2-N)/N}$ so that it vanishes for monolayer graphene ($N = 1$), is constant for BLG ($N = 2$) and diverges for thicker systems ($N > 2$). This yields the important fact[10] that the electron–electron interactions, modelled as a coupling constant in a renormalization group theory, become more and more relevant with increasing N and drive the spontaneous chiral symmetry breaking. Theoretically, this amounts to producing a spontaneous gap term in the quasiparticle Hamiltonian: $H_{\mathrm{int}} = H + m\sigma_z$. The gapless nematic states, which add mean-field terms proportional to σ_x or σ_y to the Hamiltonian, were shown to be disfavoured in theory[20,21] and thus will not be considered below. Depending on the projected sign of m at each spin valley, a family of five competing broken-symmetry phases were predicted[6,8]: the quantum valley Hall (QVH) state, the QAH state, the layer antiferromagnetic (LAF) state, the quantum spin Hall (QSH) state and the ALL state, as summarized in Fig. 1a. They exhibit distinct Hall conductivities, orbital magnetizations and layer polarizations. When magnetization and/or layer polarization are coupled to electric and/or magnetic fields, a particular state may be favoured[6,9].

In the experimental identification of these competing ordered states, we benefit from the high sample cleanliness (Supplementary Section 2) and low dielectric surrounding of freestanding samples, which maximize the interaction effects in r-TLG. Figure 1b shows an optical microscopy image of a suspended, dual-gated r-TLG device. Figure 1c shows its scattering scanning near-field optical microscopy image, which confirms the stacking order homogeneity of the sample (Supplementary Section 3). An overview of all r-TLG devices used in this study is given in Supplementary Table 1. Figure 1d–g shows the two-terminal differential conductance G as a function of the top and bottom gate voltages (V_T and V_B, respectively) and of the electric and magnetic fields (E and B, respectively).

We first discuss our observations at elevated magnetic fields, where the spontaneously gapped states introduced above adiabatically evolve into symmetry-broken quantum Hall states[22]. Indeed, at

https://doi.org/10.1038/s41567-023-02327-6

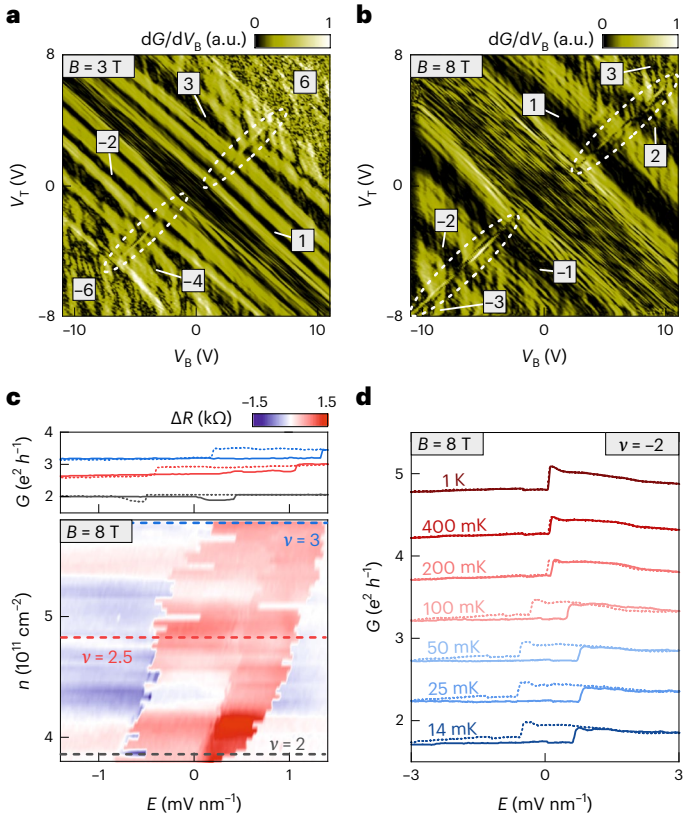

Fig. 2 | Electric hysteresis of quantum Hall ferromagnets. a,**b**, Derivative of the conductance maps shown in Fig. 1e,f, respectively, with respect to the bottom gate voltage. Landau-level filling factors are indicated by numerals. The discontinuities at vanishing electric field are highlighted by white dotted ellipses. **c**, Map of the resistance difference ΔR between forward and backward sweeps across the transition line shown in **b** as a function of electric field E and charge carrier density n at $B = 8$ T. Line cuts of forward (solid) and backward (dotted) sweeps at filling factors $\nu = 2$, 2.5 and 3 are shown in the top panel. **d**, Forward (solid) and backward (dotted) sweeps at $\nu = -2$ and $B = 8$ T for different temperatures between 14 mK (blue) and 1 K (red). The lines are offset by 0.5 $e^2 h^{-1}$ with respect to each other for clarity.

$B = 3$ T, the 12-fold degeneracy of the zero-energy Landau levels[23] is already fully broken and all plateaus at integer filling factors $-6 \le \nu \le 6$ are well resolved (Fig. 1e). This underscores the high device quality and the strong influence of exchange interaction in the system. Although such symmetry-broken states have been described previously[23,24], we observe surprisingly sharp discontinuities in the conductance within a constant filling factor close to the $E = 0$ line at $B = 8$ T (indicated by black arrows in Fig. 1f). Although the discontinuities are difficult to identify in the conductance maps, they become apparent after differentiation of Fig. 1e,f with respect to the bottom gate voltage, as shown in Fig. 2a,b. Here, the discontinuities are visible as sharp lines of high derivative, whereas the quantum Hall plateaus appear as regions with vanishing derivative. The discontinuities are present in all the symmetry-broken states with $0 < |\nu| < 6$ and are clearly visible even at $B = 3$ T (Fig. 2a). Because the top and bottom layers of r-TLG are expected to have different effective couplings to the metallic contacts, such a discontinuous jump in conductivity reflects the layer polarization of a symmetry-broken state that reverses across the $E = 0$ line. To investigate this inversion of layer polarization, several measurements sweeping across the layer-polarization transitions at different filling factors and different temperatures, but constant charge carrier densities, for $B = 8$ T are shown in Fig. 2c,d (see also Extended Data Fig. 1). Near the sharp transitions (Fig. 2c), an extremely small change in electric field of less than 50 μV nm^{-1} determines the spontaneous layer polarization between the two outermost layers, indicating ferroelectric quantum Hall states. This is in stark contrast to the observation in BLG, in which similar transitions occur at finite electric fields or extend over a broad transition region of several mV nm^{-1} with increased conductance[9,25–28]. Moreover, the transitions in r-TLG show a pronounced electric hysteresis, as shown in the line traces in the top panel of Fig. 2c. This hysteresis vanishes at temperatures above 400 mK (Fig. 2d). Unlike the case of AlAs quantum wells[29], we do not find resistive spikes at the first-order quantum phase transitions, consistent with the absence of dissipation: owing to the coincidence of layer and valley degrees of freedom[22], the counterpropagating edge modes between domains of oppositely layer-polarized quantum Hall states are localized at opposite valleys and most likely not fully gapped.

Hereafter we focus on the low-magnetic-field regime. At zero magnetic field but high electric fields, in agreement with single-particle theories[6,18,19] and previous experiments[30,31], the opening of a bandgap is evidenced by a decrease in conductance, as indicated by the red line trace in Fig. 1d. This again confirms the rhombohedral stacking order, as such a bandgap opening is impossible for Bernal TLG[17,19,30,32,33]. However, unexpected from the single-particle picture, instead of monotonously increasing with decreasing the electric field, the conductance drops again at small electric fields, indicating the opening of a spontaneous energy gap due to the electron–electron interactions[6–8]. This is consistent with the first transport spectroscopy measurements on r-TLG[34] that showed a similar spontaneous gap at vanishing electric fields, although no gap closing (and reopening) by electric field was observed. To explain this spontaneously gapped phase, Fig. 1g shows the conductance as a function of the electric and magnetic fields at charge neutrality. Clearly, the phase can be suppressed by the electric field but strengthened by the magnetic field. This observation agrees well with theoretical predictions[6–8] and previous measurements on rhombohedral graphene few-layers[17,28,34–36], and enables the identification of the emergent phase at vanishing electric fields (phase I) as a LAF state (or a canted antiferromagnetic (CAF) state at finite magnetic fields[8,34,37]). The QSH state can be excluded, considering that its protected edge states would lead to at least 2 $e^2 h^{-1}$ two-terminal conductance (see Supplementary Section 4 for more details). With increasing electric field, the layer-balanced LAF/CAF state becomes unstable towards a fully layer-polarized QVH state (phase II). The two transition lines between the CAF and QVH states are marked by an increase in conductance and become linear at high magnetic fields. This observation is in harmony with theoretical predictions[7,38,39] and previous measurements[25,26,28,40–42] on BLG. Note that the transition lines are very sharp, indicating the absence of an extra intermediate metallic phase proposed in BLG[43] and the absence of several domains[28] within the device. This is consistent with the more divergent DOS, the stronger interaction effects, and thus a larger spontaneous gap in r-TLG at charge neutrality, as compared with BLG. Similar to the case of BLG, signatures for other interaction-driven phases can be observed at low magnetic and electric fields[9,25,44]. As shown in the inset of Fig. 1g, indications of a local conductance minimum at a (negative) constant electric field can be observed in all devices. Thus, we examine the remaining spontaneously gapped phases below to shed light on the as yet unknown ground states at vanishing fields and charge carrier densities.

Figure 3a,b shows the differential conductance as a function of charge carrier density and electric field at $B = 0.2$ and 0.5 T. In addition, fan diagrams down to $B = 0$ were recorded at various electric fields, as exemplified by Fig. 3c. Distinct quantum Hall plateaus at $\nu = 0, \pm 3, \pm 6$ together with several fainter plateaus at $\nu = -1, -2, -4$ and -5 are readily identifiable even at these weak magnetic fields (Fig. 3c). The insulating $\nu = 0$ state can again be identified as the CAF state (I) that transitions to the two QVH states (II) at high electric fields. In agreement with the previous observations, the critical electric field at which the transition occurs shifts towards higher electric fields with increasing magnetic

https://doi.org/10.1038/s41567-023-02327-6

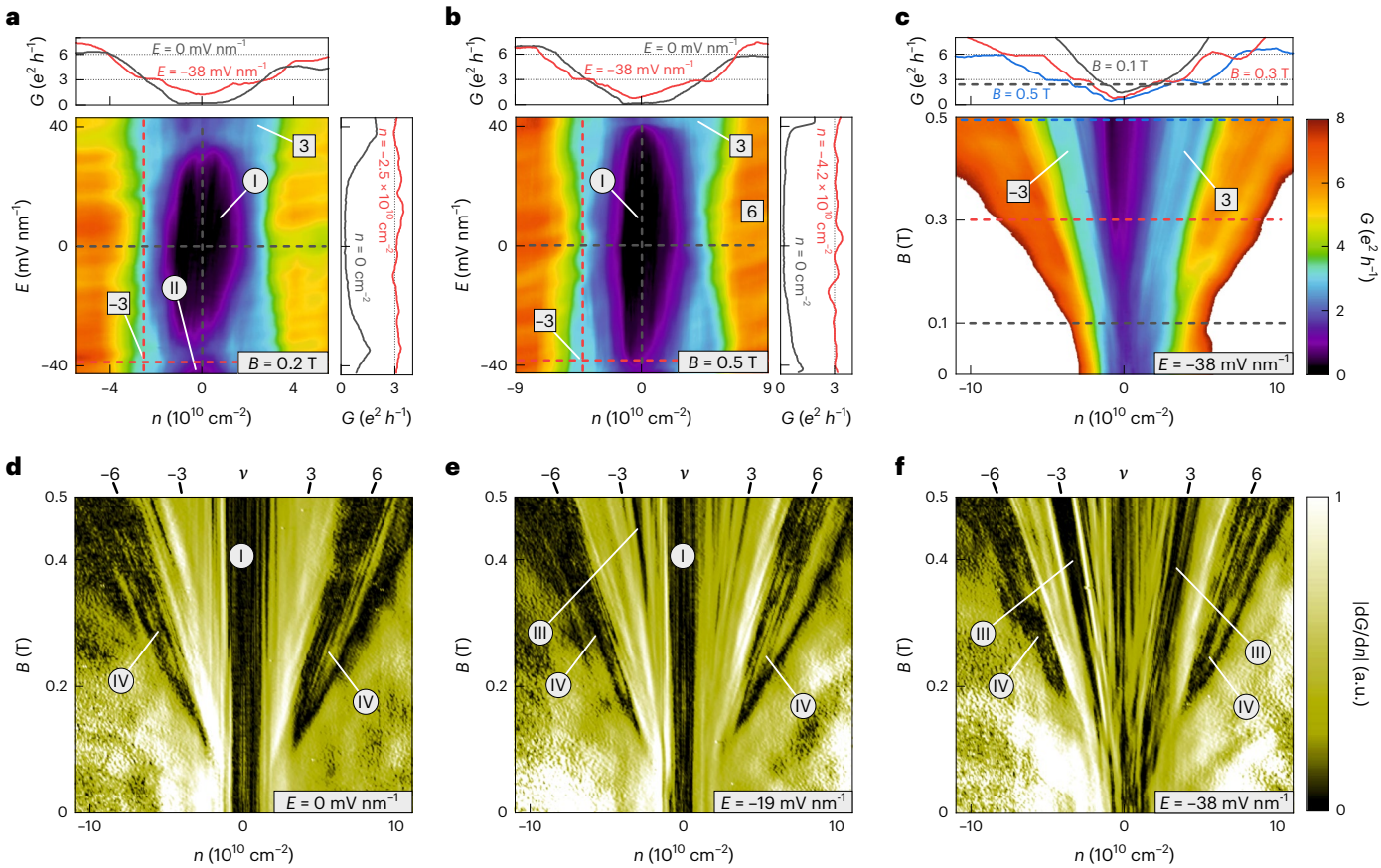

Fig. 3 | Anomalous quantum Hall states at low magnetic fields. a,**b**, Differential conductance map as a function of electric field E and charge carrier density n at $B = 0.2$ T (**a**) and $B = 0.5$ T (**b**). The top and right panels show the conductance along lines of constant E and constant n, respectively, as indicated by the dotted lines in the main panels. **c**, Fan diagram of the differential conductance at $E = -38$ mV nm^{-1}. The top panel shows the conductance along lines of constant B, as indicated by the dotted lines in the main panel. **d**–**f**, Fan diagrams of the derivative of the conductance with respect to n at $E = 0$ mV nm^{-1} (**d**), $E = -19$ mV nm^{-1} (**e**) and $E = -38$ mV nm^{-1} (**f**). The filling factors and their corresponding slopes are indicated on the top of each panel. The roman numerals indicate the predicted spontaneous quantum Hall states, namely, the LAF/CAF (I), QVH (II), ALL (III) and QAH (IV) states.

field (Fig. 1g). The observation of prominent plateaus at $\nu = \pm 6$ and especially $\nu = \pm 3$ at these low magnetic fields, however, is unconventional (similar $\nu = \pm 6$ states can even be observed in an hexagonal boron nitride screened device[15]). Remarkably, the $\nu = \pm 6$ states show only a weak electric field dependence and are visible at zero electric field, whereas the $\nu = \pm 3$ states stabilize at finite electric fields only.

To track these quantum Hall states to lower magnetic fields, it is instructive to examine the derivative of the fan diagram with respect to charge carrier density, as shown in Fig. 3d–f (see Extended Data Fig. 2 for further data). In such a diagram, quantum Hall plateaus appear as regions with vanishing derivative. In addition, in their vicinity features with the same slope are visible that correspond to fluctuations near incompressible quantum states. These states are indicative of an energy gap and allow to identify emerging quantum Hall states even before their signature is visible in conventional magneto-transport measurements[9,44,45]. At zero electric field (Fig. 3d), the $\nu = \pm 3$ states are absent whereas the $\nu = \pm 6$ states persist down to approximately 100 mT. With increasing electric field, the $\nu = \pm 3$ states become more and more distinct and even stabilize at exceptionally low magnetic fields of less than 50 mT. Note that the LAF/CAF state at $\nu = 0$ is visible only at higher magnetic fields in Fig. 3f, because the chosen electric field is close to the critical value for the LAF-QVH phase transition (Fig. 1g). Overall, compared to the aforementioned theory, the observations align well with the stabilization of the ALL (III) and QAH (IV) states that were predicted[6] to have Chern numbers ±3 and ±6, respectively, as featured in Fig. 1a. Because they have non-trivial orbital magnetization[6,8], both states are expected to be favoured in external magnetic fields. Moreover, as the ALL state is partially spin- and, in particular, layer-polarized[6,8], the $\nu = \pm 3$ states are expected to be favoured in electric fields. Our observations are indeed consistent with these predicted properties.

To shed more light on the nature of the spontaneous quantum Hall states and to examine their competition for the ground state, the two-terminal conductance at various different filling factors was tracked while sweeping the magnetic field through zero. As the QAH and ALL states both exhibit orbital magnetism[6,8], they are expected to show hysteretic behaviour in the longitudinal and Hall conductances[1–3]. The same is true for the two-terminal conduction that contains contributions from both conductances. (Although indications of magnetism in rhombohedral graphene have been observed previously, their origins are irrelevant to the QAH and ALL states[17,36] as they did not trace these states by fixing the filling factors.) Figure 4a,c features the conductance as functions of magnetic field for both forward and backward sweeps at constant filling factors at $E = -20$ mV nm^{-1}. For comparison, Fig. 4b shows the conductance at constant charge carrier densities, that is, varying filling factors. In all cases, forward and backward sweeps are mirror symmetric with respect to $B = 0$. First, noticeable hysteresis can be evidenced at filling factors close to the $\nu = -3$ and the $\nu = -6$ states, whereas it is absent at filling factors far away, for example, $\nu = 0$ and $\nu = -8$ (Fig. 4c). Second, there is no noticeable hysteresis at any fixed charge carrier density (Fig. 4b). These hysteretic features are consistent with the stabilization of the QAH state at $\nu = \pm 6$ and the ALL state at $\nu = \pm 3$. However, the fact that their conductances

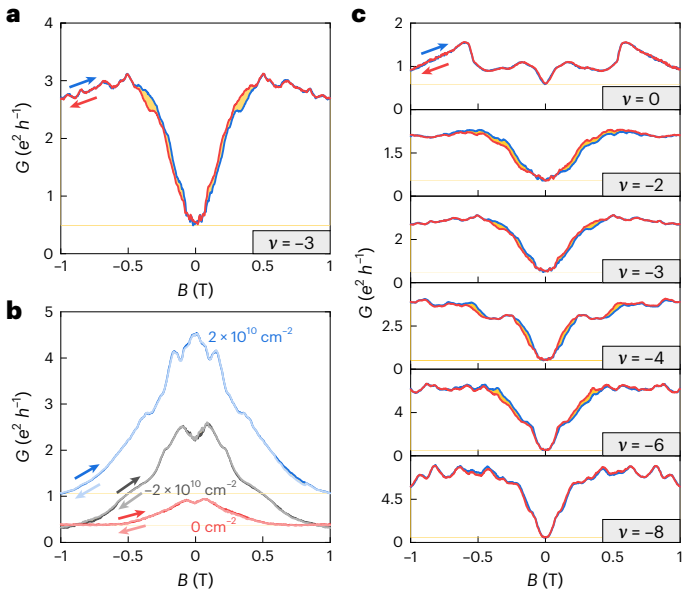

Fig. 4 | Magnetic hysteresis at a constant electric field $E = -20$ mV nm^{-1}. **a**, Conductance as a function of magnetic field B at the filling factor $\nu = -3$. The hysteresis loop area formed by the forward (blue) and backward (red) sweeps is shaded in yellow. **b**, Conductance as a function of B at the densities $n = -2 \times 10^{10}$ cm^{-2} (black), $n = 0$ cm^{-2} (red) and $n = 2 \times 10^{10}$ cm^{-2} (blue). The forward and backward sweeps are indicated in dark and bright colours, respectively. **c**, Similar to **a**, but for a sequence of filling factors ranging from $\nu = 0$ to $\nu = -8$. Here the y axis was rescaled for each filling factor to enhance the visibility of hysteresis.

drop to values below 1 $e^2 h^{-1}$ at $B = 0$ implies that there are no percolating edge states at $B = 0$, and that both states lose the competition against the LAF or QVH state at $B = 0$. Besides, it has also been pointed out for similar devices that the current annealing-induced disorder close to the electrical contacts could hinder the coupling between edge channels and electrical contacts, thereby obscuring the observation of conductance at $B = 0$ (ref. 46). In this scenario, the magnetic hysteresis supported QAH state near zero electric field and ALL state at elevated electric fields might persist down to $B = 0$, although they cannot be accessed by two-terminal transport measurements.

Although future study using multi-terminal devices with still higher quality is necessary to unveil the fate of the QAH, ALL and ferroelectric states at strictly $B = 0$, our findings underscore that the natural rhombohedral graphene systems are fertile grounds for intrinsically interacting electron physics with no need of the delicate moiré engineering[6,19] large electric fields or hexagonal boron nitride encapsulation.

Online content

Any methods, additional references, Nature Portfolio reporting summaries, source data, extended data, supplementary information, acknowledgements, peer review information; details of author contributions and competing interests; and statements of data and code availability are available at https://doi.org/10.1038/s41567-023-02327-6.

References

1. Sharpe, A. L. et al. Emergent ferromagnetism near three-quarters filling in twisted bilayer graphene. *Science* **365**, 605–608 (2019).
2. Serlin, M. et al. Intrinsic quantized anomalous Hall effect in a moiré heterostructure. *Science* **367**, 900–903 (2020).
3. Polshyn, H. et al. Electrical switching of magnetic order in an orbital Chern insulator. *Nature* **588**, 66–70 (2020).
4. Chen, G. et al. Tunable correlated Chern insulator and ferromagnetism in a moiré superlattice. *Nature* **579**, 56–61 (2020).
5. Tschirhart, C. L. et al. Imaging orbital ferromagnetism in a moiré Chern insulator. *Science* **372**, 1323–1327 (2021).
6. Zhang, F., Jung, J., Fiete, G. A., Niu, Q. & MacDonald, A. H. Spontaneous quantum Hall states in chirally stacked few-layer graphene systems. *Phys. Rev. Lett.* **106**, 156801 (2011).
7. Nandkishore, R. & Levitov, L. Flavor symmetry and competing orders in bilayer graphene. Preprint at https://arxiv.org/abs/1002.1966 (2010).
8. Zhang, F. Spontaneous chiral symmetry breaking in bilayer graphene. *Synth. Met.* **210**, 9–18 (2015).
9. Geisenhof, F. R. et al. Quantum anomalous Hall octet driven by orbital magnetism in bilayer graphene. *Nature* **598**, 53–58 (2021).
10. Zhang, F., Min, H. & MacDonald, A. H. Competing ordered states in bilayer graphene. *Phys. Rev. B* **86**, 155128 (2012).
11. Zhou, H. et al. Isospin magnetism and spin-polarized superconductivity in Bernal bilayer graphene. *Science* **375**, 774–778 (2022).
12. Zhang, Y. et al. Enhanced superconductivity in spin-orbit proximitized bilayer graphene. *Nature* **613**, 268–273 (2023).
13. La Barrera et al. Cascade of isospin phase transitions in Bernal-stacked bilayer graphene at zero magnetic field. *Nat. Phys.* **18**, 771–775 (2022).
14. Seiler, A. M. et al. Quantum cascade of correlated phases in trigonally warped bilayer graphene. *Nature* **608**, 298–302 (2022).
15. Zhou, H. et al. Half- and quarter-metals in rhombohedral trilayer graphene. *Nature* **598**, 429–433 (2021).
16. Zhou, H., Xie, T., Taniguchi, T., Watanabe, K. & Young, A. F. Superconductivity in rhombohedral trilayer graphene. *Nature* **598**, 434–438 (2021).
17. Shi, Y. et al. Electronic phase separation in multilayer rhombohedral graphite. *Nature* **584**, 210–214 (2020).
18. Koshino, M. & McCann, E. Trigonal warping and Berry's phase Nπ in ABC-stacked multilayer graphene. *Phys. Rev. B* **80**, 165409 (2009).
19. Zhang, F., Sahu, B., Min, H. & MacDonald, A. H. Band structure of ABC-stacked graphene trilayers. *Phys. Rev. B* **82**, 035409 (2010).
20. Jung, J. & MacDonald, A. H. Gapped broken symmetry states in ABC-stacked trilayer graphene. *Phys. Rev. B* **88**, 075408 (2013).
21. Cvetkovic, V. & Vafek, O. Topology and symmetry breaking in ABC trilayer graphene. Preprint at https://arxiv.org/abs/1210.4923 (2012).
22. Zhang, F., Tilahun, D. & MacDonald, A. H. Hund's rules for the N=0 Landau levels of trilayer graphene. *Phys. Rev. B* **85**, 165139 (2012).
23. Lee, Y. et al. Multicomponent quantum Hall ferromagnetism and Landau level crossing in rhombohedral trilayer graphene. *Nano Lett.* **16**, 227–231 (2016).
24. Zhang, L., Zhang, Y., Camacho, J., Khodas, M. & Zaliznyak, I. The experimental observation of quantum Hall effect of l=3 chiral quasiparticles in trilayer graphene. *Nat. Phys.* **7**, 953–957 (2011).
25. Weitz, R. T., Allen, M. T., Feldman, B. E., Martin, J. & Yacoby, A. Broken-symmetry states in doubly gated suspended bilayer graphene. *Science* **330**, 812–816 (2010).
26. Velasco, J. et al. Competing ordered states with filling factor two in bilayer graphene. *Nat. Commun.* **5**, 4550 (2014).
27. Pan, C. et al. Layer polarizability and easy-axis quantum Hall ferromagnetism in bilayer graphene. *Nano Lett.* **17**, 3416–3420 (2017).
28. Geisenhof, F. R. et al. Impact of electric field disorder on broken-symmetry states in ultraclean bilayer graphene. *Nano Lett.* **22**, 7378–7385 (2022).
29. De Poortere, E. P., Tutuc, E., Papadakis, S. J. & Shayegan, M. Resistance spikes at transitions between quantum Hall ferromagnets. *Science* **290**, 1546–1549 (2000).

30. Zou, K., Zhang, F., Clapp, C., MacDonald, A. H. & Zhu, J. Transport studies of dual-gated ABC and ABA trilayer graphene. Band gap opening and band structure tuning in very large perpendicular electric fields. *Nano Lett.* **13**, 369–373 (2013).
31. Lui, C. H., Li, Z., Mak, K. F., Cappelluti, E. & Heinz, T. F. Observation of an electrically tunable band gap in trilayer graphene. *Nat. Phys.* **7**, 944–947 (2011).
32. Aoki, M. & Amawashi, H. Dependence of band structures on stacking and field in layered graphene. *Solid State Commun.* **142**, 123–127 (2007).
33. Koshino, M. Interlayer screening effect in graphene multilayers with ABA and ABC stacking. *Phys. Rev. B* **81**, 125304 (2010).
34. Lee, Y. et al. Competition between spontaneous symmetry breaking and single-particle gaps in trilayer graphene. *Nat. Commun.* **5**, 5656 (2014).
35. Myhro, K. et al. Large tunable intrinsic gap in rhombohedral-stacked tetralayer graphene at half filling. *2D Mater.* **5**, 45013 (2018).
36. Lee, Y. et al. Gate tunable magnetism and giant magnetoresistance in ABC-stacked few-layer graphene. Preprint at https://arxiv.org/abs/1911.04450 (2019).
37. Zhang, F. & MacDonald, A. H. Distinguishing spontaneous quantum Hall states in bilayer graphene. *Phys. Rev. Lett.* **108**, 186804 (2012).
38. Kharitonov, M. Canted antiferromagnetic phase of the $\nu=0$ quantum Hall state in bilayer graphene. *Phys. Rev. Lett.* **109**, 046803 (2012).
39. Kharitonov, M. Antiferromagnetic state in bilayer graphene. *Phys. Rev. B* **86**, 195435 (2012).
40. Bao, W. et al. Evidence for a spontaneous gapped state in ultraclean bilayer graphene. *Proc. Natl Acad. Sci. USA* **109**, 10802–10805 (2012).
41. Velasco, J. et al. Transport spectroscopy of symmetry-broken insulating states in bilayer graphene. *Nat. Nanotech.* **7**, 156–160 (2012).
42. Freitag, F., Weiss, M., Maurand, R., Trbovic, J. & Schönenberger, C. Spin symmetry of the bilayer graphene ground state. *Phys. Rev. B* **87**, 161402 (2013).
43. Li, J. et al. Metallic phase and temperature dependence of the $\nu=0$ quantum Hall state in bilayer graphene. *Phys. Rev. Lett.* **122**, 097701 (2019).
44. Martin, J., Feldman, B. E., Weitz, R. T., Allen, M. T. & Yacoby, A. Local compressibility measurements of correlated states in suspended bilayer graphene. *Phys. Rev. Lett.* **105**, 256806 (2010).
45. Lee, D. S., Skákalová, V., Weitz, R. T., von Klitzing, K. & Smet, J. H. Transconductance fluctuations as a probe for interaction-induced quantum Hall states in graphene. *Phys. Rev. Lett.* **109**, 056602 (2012).
46. Freitag, F., Weiss, M., Maurand, R., Trbovic, J. & Schönenberger, C. Homogeneity of bilayer graphene. *Solid State Commun.* **152**, 2053–2057 (2012).

Methods

Sample preparation

r-TLG flakes were exfoliated onto a Si wafer with a 300 nm SiO_2 layer and identified by optical microscopy, Raman spectroscopy and atomic force microscopy. In addition, scattering scanning near-field optical microscopy was used to ensure stacking order homogeneity down to nanometre scale and to confirm the absence of any structural (ABC–ABA) domain walls[47] (see also Supplementary Section 3). Suspended dual-gated structures were fabricated as follows. First, regions with homogeneous stacking order were cut out using standard electron-beam lithography together with reactive-ion etching to prevent a rhombohedral to Bernal stacking transition[47]. Electrical contacts (5/100 nm Cr/Au), a 140 nm SiO_2 spacer and the top gate (5/160 nm Cr/Au) were fabricated consecutively using electron-beam lithography. To decrease the contact resistance, contacts were treated in a ultraviolet/ozone environment for 1 min before metal evaporation. Subsequently, samples were submersed in buffered hydrofluoric acid to remove the SiO_2 spacer and 150 nm of the SiO_2 below the r-TLG flake. The devices were transferred to ethanol and dried in a critical point dryer to prevent collapse of the suspended graphene devices. A schematic of a suspended device is shown in Extended Data Fig. 3.

Quantum transport

All measurements were performed in a dilution refrigerator at temperatures below 10 mK (unless specified otherwise) using a standard lock-in technique at an a.c. frequency of 78 Hz and currents below 5 nA. Before any measurement, the devices were cleaned in situ by current annealing (Supplementary Section 5). By adjusting the voltages V_B and V_T of the silicon back gate and the gold top gate, respectively, both the charge carrier density $n = C_B(\alpha V_T + V_B)/e$ and the electric field $E = C_B(\alpha V_T - V_B)/2\varepsilon_0$ could be tuned independently[25]. Here, C_B is the capacitance per unit area of the bottom gate, α is the ratio of top and bottom gate capacitances $\alpha = C_T/C_B$, e is the electron charge and ε_0 is the vacuum permittivity. The calibration procedure is outlined in Supplementary Section 6. The contact resistance R_C and the bottom gate capacitance were extracted from the quantum Hall plateaus at $B = 3$ T and various electric fields.

Data availability

Original data are available in the Göttingen Research Online Data repository (GRO.data) at https://doi.org/10.25625/VXUMPN.

References

47. Geisenhof, F. R. et al. Anisotropic strain-induced soliton movement changes stacking order and band structure of graphene multilayers. Implications for charge transport. *ACS Appl. Nano Mater.* **2**, 6067–6075 (2019).

Acknowledgements

F.W., F.R.G., N. F. and R.T.W. acknowledge funding from the Center for Nanoscience (CeNS) and by the Deutsche Forschungsgemeinschaft (DFG, German Research Foundation) under Germany's Excellence Strategy-EXC-2111-390814868 (MCQST). R.T.W. acknowledges partial funding from the DFG SPP 2244 (2DMP). F.Z. acknowledges support from the US National Science Foundation under grant numbers DMR-1945351 through the CAREER programme, DMR-2105139 through the CMP programme and DMR-2324033 through the DMREF programme.

Author contributions

F.W., F.R.G. and N.F. fabricated the samples. F.W. and N.F. conducted the electrical measurements with the help of A.M.S. and F.R.G. F.Z. developed the theory. All authors discussed and interpreted the data. The paper was written by F.W, F.Z. and R.T.W., with input from all authors.

Competing interests

The authors declare no competing interests.

Additional information

Extended data is available for this paper at https://doi.org/10.1038/s41567-023-02327-6.

Supplementary information The online version contains supplementary material available at https://doi.org/10.1038/s41567-023-02327-6.

Correspondence and requests for materials should be addressed to Fan Zhang or R. Thomas Weitz.

Peer review information *Nature Physics* thanks the anonymous reviewers for their contribution to the peer review of this work.

https://doi.org/10.1038/s41567-023-02327-6

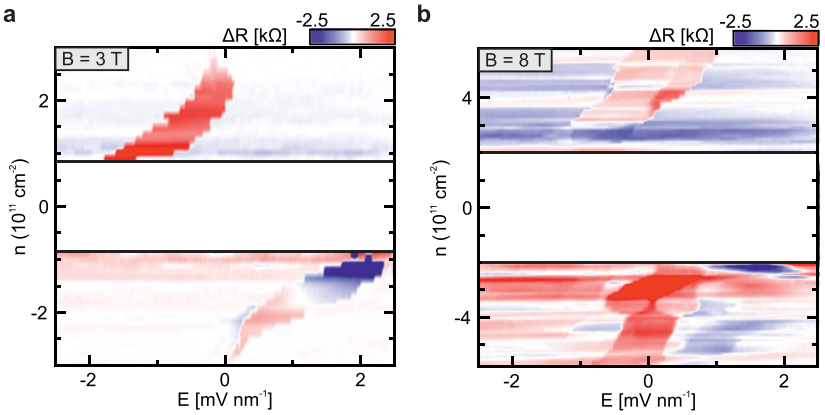

Extended Data Fig. 1 | Ferroelectric states. a,**b**, Map of the resistance difference between forward and backward sweep of the electric field as function of electric field and charge carrier density at B = 3 T in **a** and B = 8 T in **b**. The region with vanishing conductance at zero density has been removed due to large resistance variations to enhance visibility.

https://doi.org/10.1038/s41567-023-02327-6

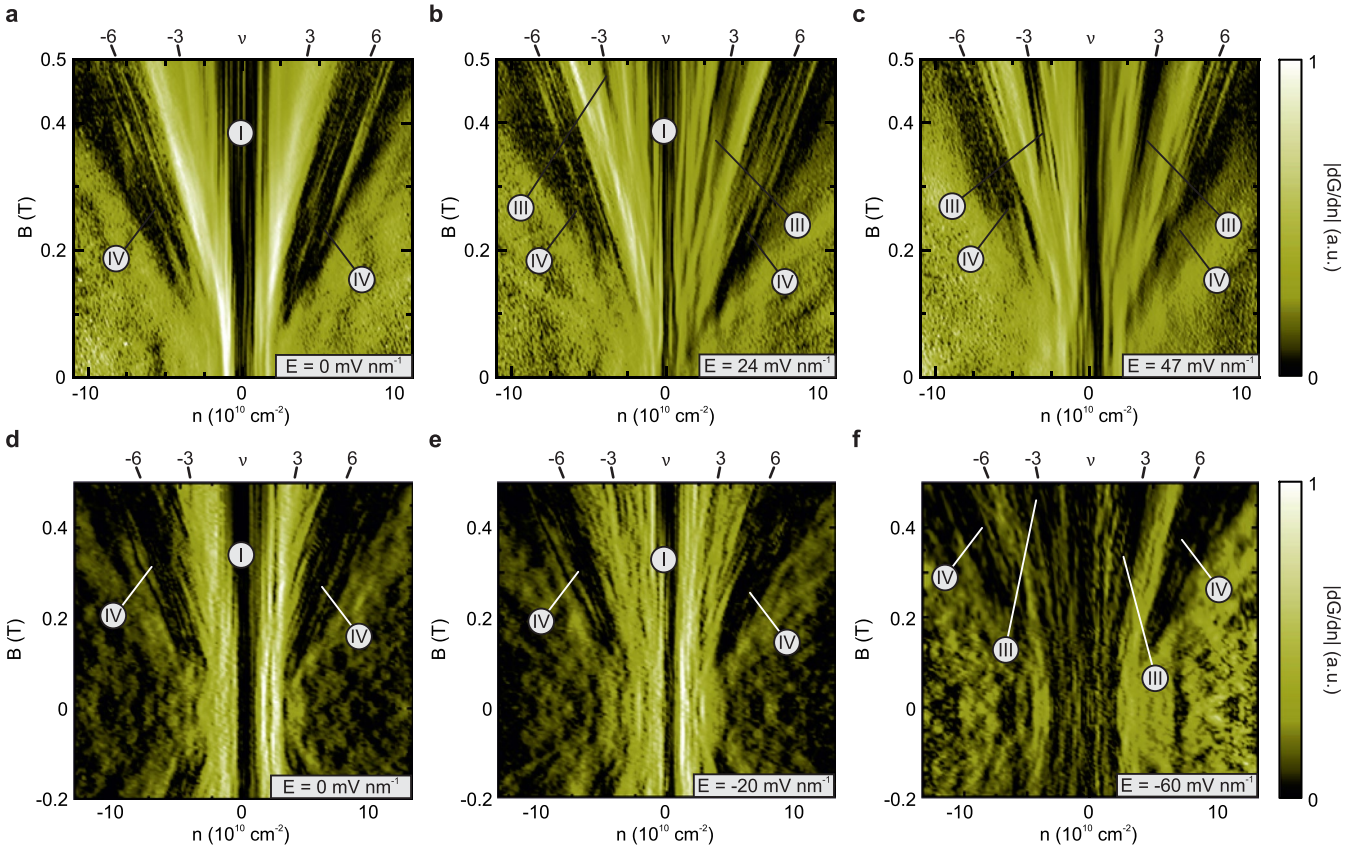

Extended Data Fig. 2 | Quantum Hall states at low magnetic fields. a-c, fan diagrams of the conductance derivative with respect to the charge carrier density of device A2 (cf. Supporting Table 1) at E = 0 mV nm^{-1} in **a**, E = 24 mV nm^{-1} in **b** and E = 47 mV nm^{-1} in **c**. The filling factors and their corresponding slopes are indicated on the top of each panel. The roman numerals indicate the associated spontaneous quantum Hall states, namely the LAF/CAF state (I), the ALL state (III) and the QAH state (IV). **d-f**, Fan diagrams of the conductance derivative with respect to the charge carrier density of device B1 (cf. Supporting Table 1) at E = 0 mV nm^{-1} in **d**, E = −20 mV nm^{-1} in **e** and E = −60 mV nm^{-1} in **f**. The filling factors and their corresponding slopes are indicated on the top of each panel.

https://doi.org/10.1038/s41567-023-02327-6

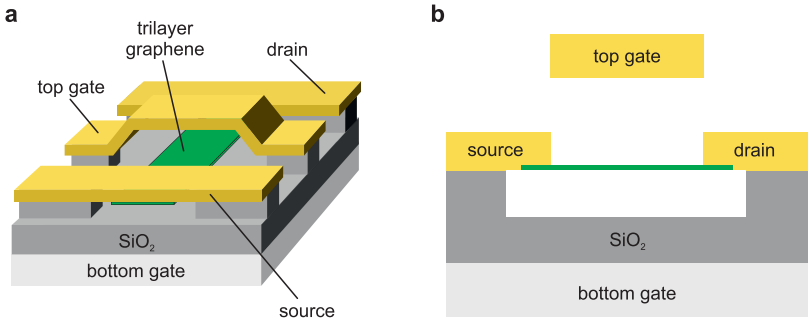

Extended Data Fig. 3 | Device schematics. a, 3D view of a dual-gated trilayer graphene device with a silicon bottom gate and a gold top gate. **b**, Cross section of the device shown in **a** along the graphene axis.